Supporting Information

Heterogeneously Integrated Graphene/Silicon/Halide Waveguide Photodetectors toward Chip-Scale Zero-Bias Long-Wave Infrared Spectroscopic Sensing

Yiming Ma,[†,‡,§,⊥] *Yuhua Chang,*[†,‡,⊥] *Bowei Dong,*[†,‡] *Jingxuan Wei,*[†,‡] *Weixin Liu,*[†,‡] *and Chengkuo Lee*[*,†,‡,§,∥]

[†]Department of Electrical and Computer Engineering, National University of Singapore, Singapore 117583, Singapore

[‡]Center for Intelligent Sensors and MEMS (CISM), National University of Singapore, Singapore 117608, Singapore

[§]NUS Suzhou Research Institute (NUSRI), Suzhou Industrial Park, Suzhou 215123, China

[∥]NUS Graduate School - Integrative Sciences and Engineering Programme (ISEP), National University of Singapore, Singapore 119077, Singapore

[⊥]Y.M. and Y.C. contributed equally.

*Email: elelc@nus.edu.sg

Contents

Note S1: PDMS stamp fabrication process

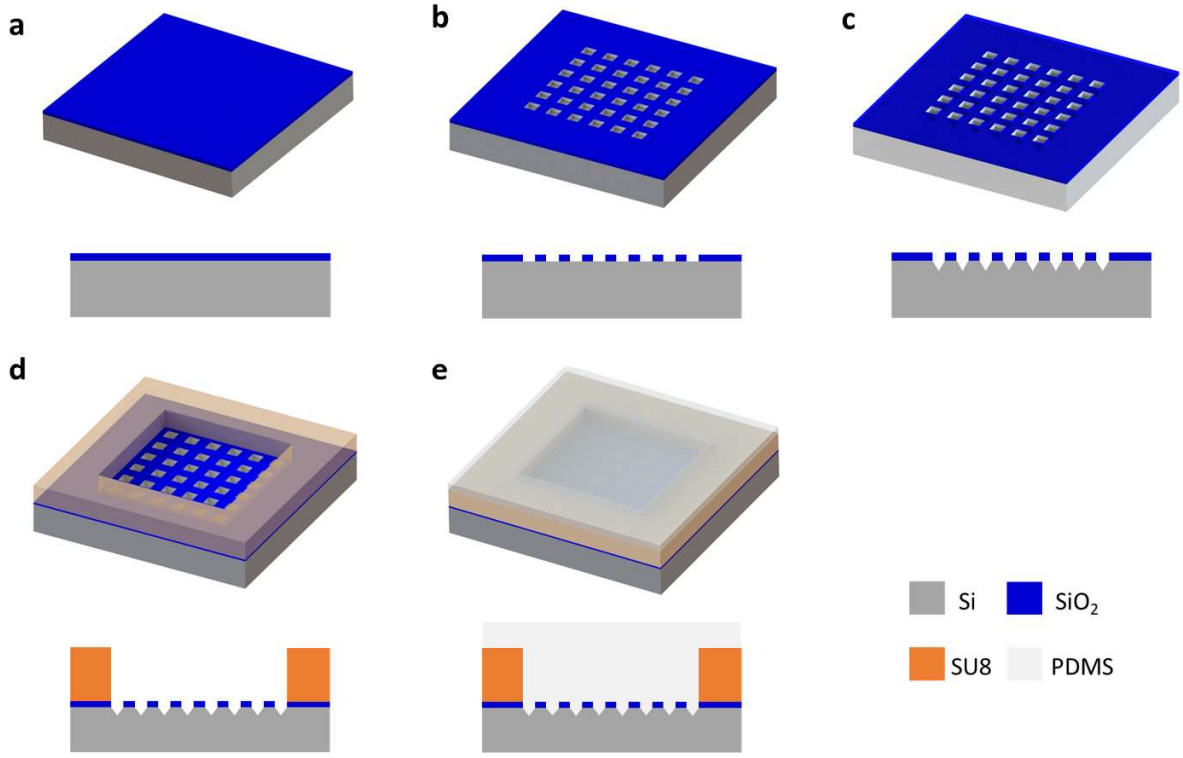

Figure S1. Fabrication process for PDMS stamp. (a) 300 nm SiO_2 on <100> Si wafer. (b) Etch 300 nm SiO_2. (c) Wet etch Si in KOH solution. (d) Expose SU8. (e) Pour PDMS base and agent into mold and cure.

The mold was fabricated from a <100> Si wafer with 300 nm SiO_2. The sample was firstly spin-coated with AZ 1514 at 6500 rpm and patterned into an array of squares with 45 μm period and 15 μm width. SiO_2 was etched by Ar/CHF_3 at 60 °C. The etching rate was around 100 nm per minute. Then <100> Si was wet etched by 30% potassium hydroxide (KOH) at 80 °C for 30 min to create the inverse pyramids with SiO_2 layer as a hard mask. Magnetic stirring is recommended otherwise air bubbles may block SiO_2 opening from KOH solution. Afterward, SU8 3050 was

spin-coated at 1000 rpm for approximately 120 μm thickness and exposed. The mold was left in the air to age for one day to facilitate demolding. Before PDMS could be poured in, the SU8 surface was further passivated by merging mold into detergent solution. The mixing ratio of PDMS base and agent was 5:1 for better elasticity. The regular 10:1 mixing ratio leads to soft microtips on the stamp, which will not bounce back to the initial state and the membrane cannot be transferred. Finally, PDMS was cured at 65 ℃ on a hot plate for 2 hours and peeled off.

Note S2: Membrane retrieval by PDMS stamp

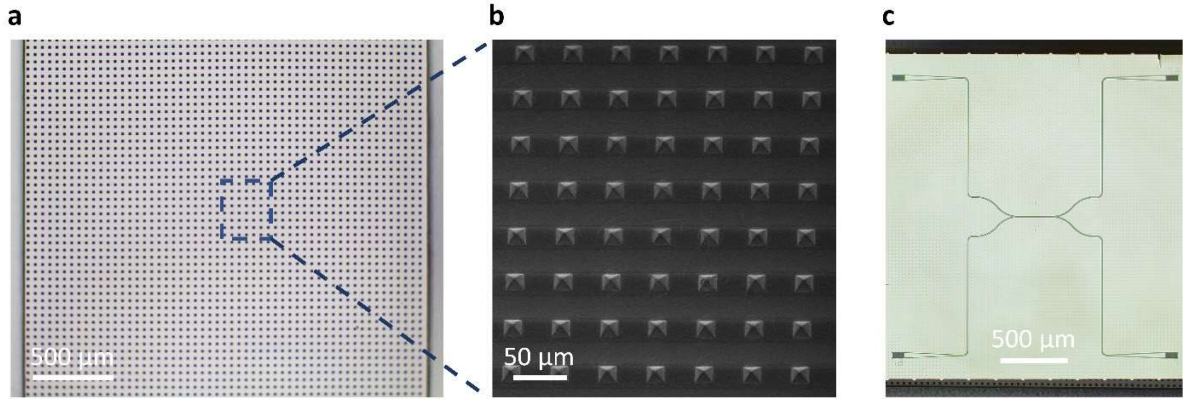

Figure S2. (a) OM image of the 2.5 mm × 2.5 mm PDMS stamp with microstructured pyramid array. (b) Zoom-in SEM image of the pyramid array. (c) OM image of a 2.4 mm × 2.4 mm Si membrane retrieved by PDMS stamp, with waveguide patterned.

Note S3: Graphene photodetector integration process

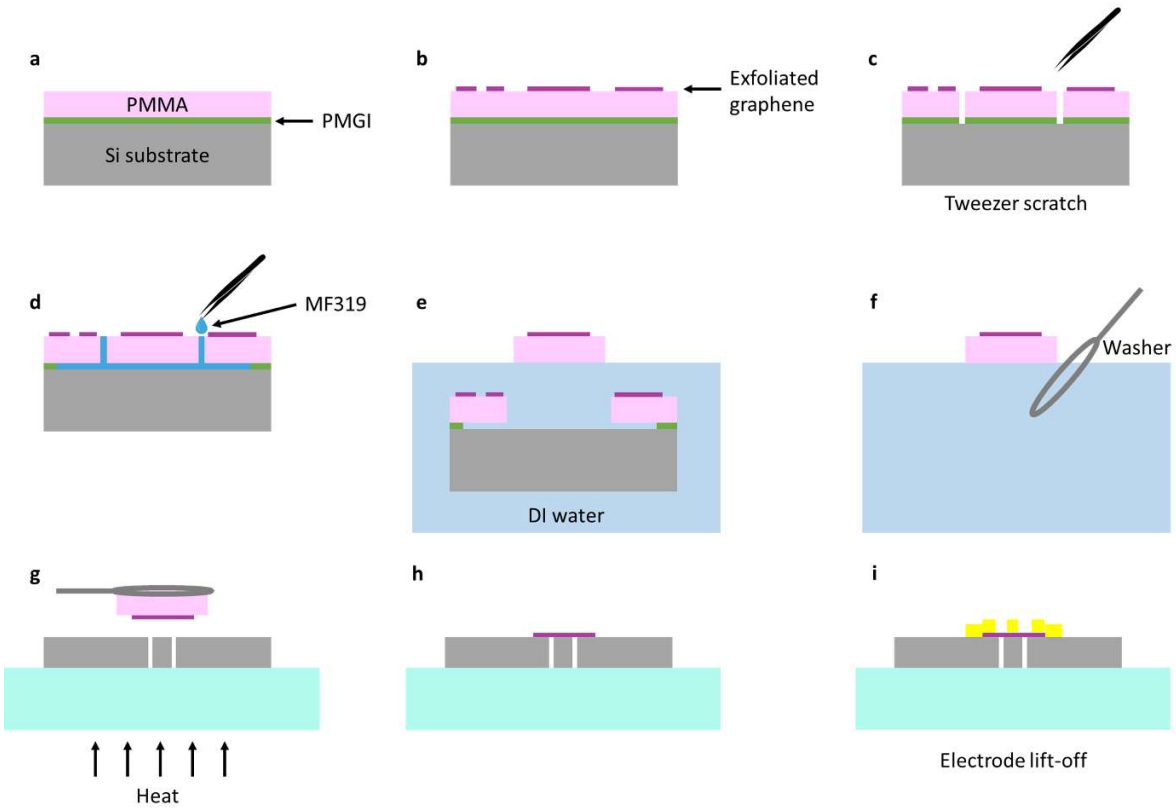

Figure S3. Graphene transfer and electrode lift-off process.

The graphene transfer process started from a silicon transfer substrate spin-coated with PMGI and PMMA. Graphene flakes were mechanically exfoliated onto the transfer substrate using typical scotch tape. After identifying the flake with suitable size and thickness by optical microscopy and Raman spectroscopy, the flake was isolated by removing a circle of resist around it using tweezer scratching. Then the PMGI layer within the circle was slowly dissolved by MF319 solution, which was delivered to the circular scratch by tweezer leveraging the capillary effect. The transfer substrate was then gently dipped in DI water with a small tilt angle. The PMMA membrane carrying the chosen graphene flake was spontaneously separated from the silicon

substrate and floated on the DI water because of the surface tension. The membrane was lifted out of the water using a washer and slowly dried by the light from the optical microscope. A homemade transfer station consisting of a microscope, a micromanipulator, and a sample stage is used to align the graphene flake with the waveguide on the target substrate. Once in contact, heat was applied to the target substrate to melt the PMMA from the washer onto the waveguide. The target substrate was then baked at 130 ℃ for 1 h to ensure good adhesion between graphene and waveguide. The PMMA residue was removed by acetone. Electrodes were patterned by e-beam lithography with PMMA as resist. Subsequently, 1 nm Ti and 70 nm Au were deposited by e-beam evaporation, followed by lift-off in acetone.

Note S4: Two grating coupler designs

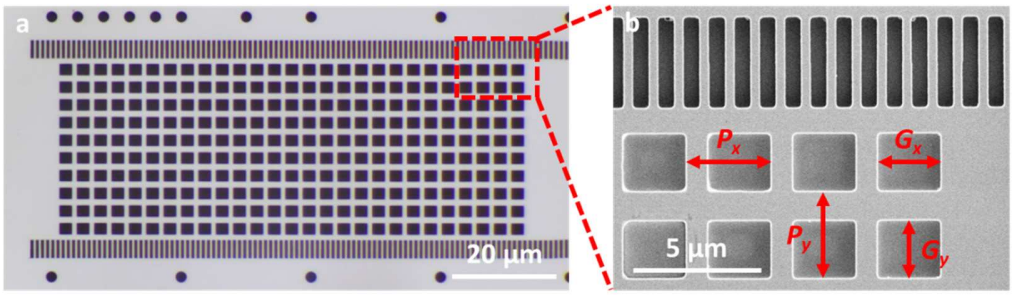

c	GC I	GC II
P_x (μm)	3.35	3.44
P_y (μm)	3.4	3.62
G_x (μm)	2.55	2.50
G_y (μm)	2.32	2.44
Central Wavelength (μm)	6.51	6.61
Max. Coupling Efficiency (dB)	-12.23	-9.77
3-dB Bandwidth (nm)	200	200

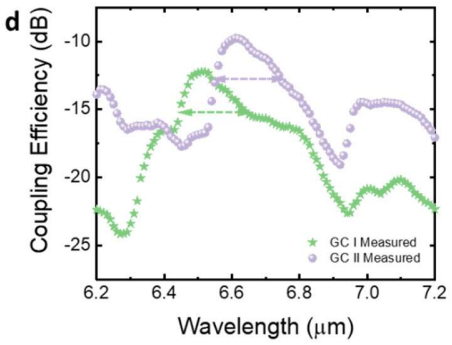

Figure S4. Two grating couplers (GCs) with different designs. (a) OM image. (b) SEM image. The four design parameters are marked. (c) Values of the four design parameters and the three measured performance parameters in the two GCs. (d) Measured coupling efficiency spectra of the two GCs. The dashed arrows indicate the 3-dB bandwidths.

Note S5: Transfer-printed waveguides

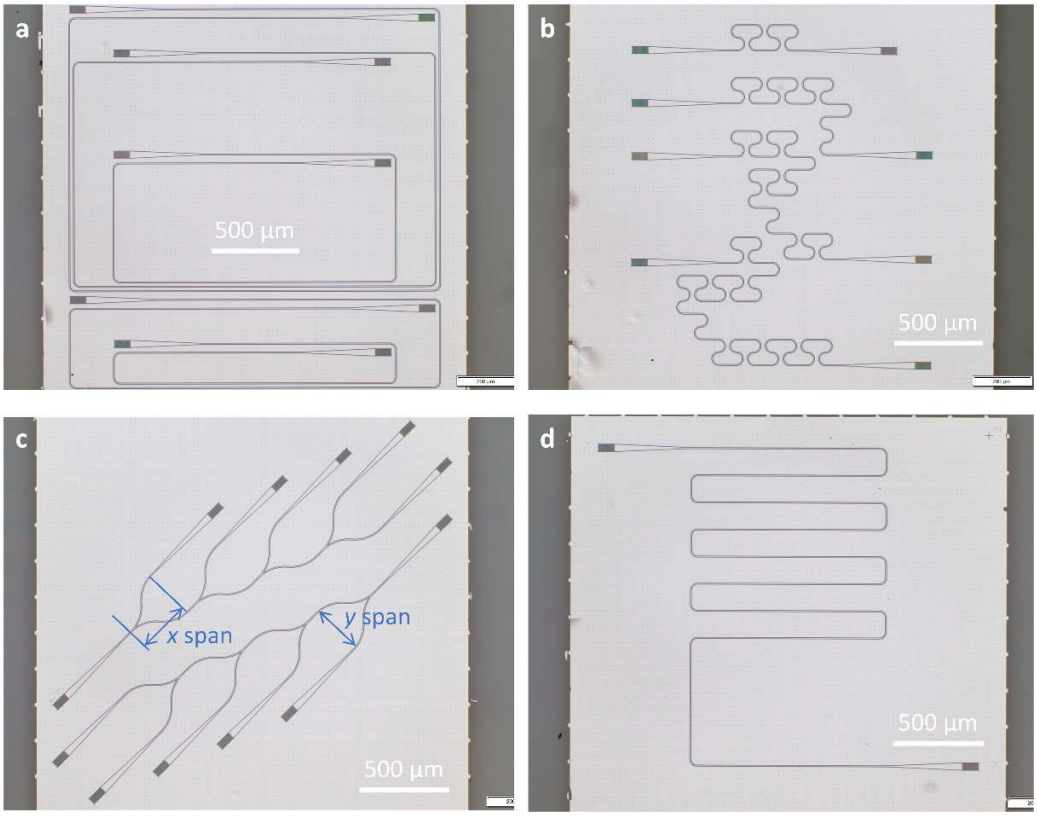

Figure S5. OM images of (a) waveguides with different lengths for cut-back measurement of propagation loss; (b) waveguides with different numbers of 90° bends for cut-back measurement of bending loss; (c) cascaded Y-junctions for cut-back characterization of Y-junction; (d) folded waveguide for sensing demonstration. The input and output grating couplers are separated by at least 1.4 mm to eliminate light coupling between the input and output fibers through surface reflection.

Note S6: Illustration of plasmonic resonance

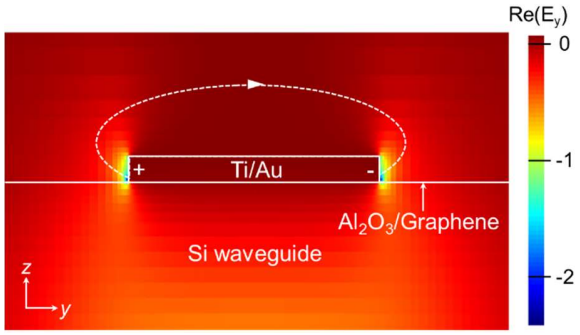

Figure S6. Distribution of Re(E_y) at the waveguide cross-section. The white dash line shows the direction of E_y.

Note S7: Raman and AFM measurements

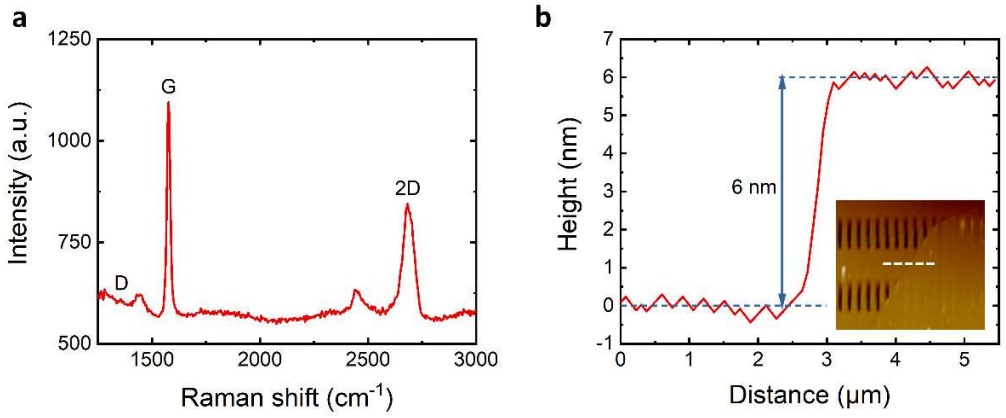

Figure S7. Graphene flake in the former waveguide-integrated graphene photodetector. (a) Raman spectrum. The stronger intensity of the G peak than that of the 2D peak suggests the graphene flake has few layers. The weak D peak suggests a relatively clean surface of graphene. (b) Flake thickness measured by AFM. Inset shows the AFM image. The white dotted line indicates the cross-section to measure the flake thickness.

Note S8: Electric field distributions with different signal electrode widths

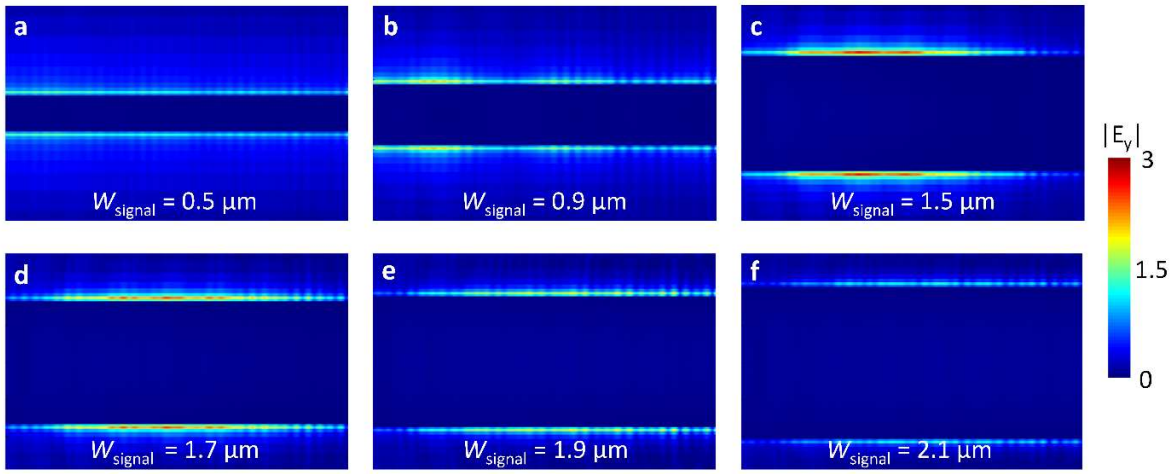

Figure S8. Simulated electric field $|E_y|$ distributions with different widths of the signal electrode at *xy* plane and at 6.51 µm.

Note S9: Discussion on waveguide thickness

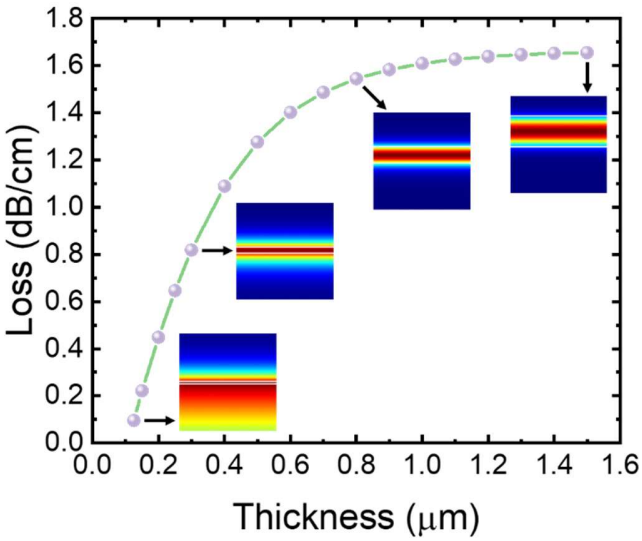

Figure S9. Simulated loss of the fundamental TE mode as a function of Si slab waveguide thickness at 7.1 μm. Insets show the mode profiles at four different Si slab waveguide thicknesses.

For SOI and suspended Si platforms, the Si waveguide needs to be thick enough to effectively suppress the optical leakage to the Si substrate. As studied in a previous work, with 3 μm BOX layer thickness, the Si waveguide thickness needs to be larger than 1.3 μm for operation at 7.67 μm wavelength.[1] In contrast, this issue does not exist in our SOCF platform since the Si waveguide directly sits on the bulk CaF_2 substrate and CaF_2 is transparent up to 8 μm. Thus, the Si waveguide thickness in the SOCF platform can be smaller. Since a wider waveguide also provides better vertical confinement, here we simulate the fundamental TE mode for a slab waveguide (*i.e.*, waveguide width → ∞) at 7.1 μm to assess the lower limit of the waveguide thickness. As shown in Figure S9, with waveguide thickness decreasing from 1.5 to 0.125 μm, the simulated loss reduces because of the lower ratio of the optical mode confined in the Si slab, resulting in lower

Si absorption loss. Further decreasing the waveguide thickness to 0.1 μm, no mode confined in the Si slab could be found.

To further estimate the cut-off waveguide thickness for a certain wavelength, we utilize Marcatili's method, which is an approximate analytical method with both simplicity and good accuracy.[2] The waveguide in our case can be divided into 5 regions as shown in Figure S10. The condition of the existence of TE mode is:

$$i < \frac{2a}{\lambda}\sqrt{n_1^2 - n_3^2} + 1 - \frac{1}{\pi}\arctan\left(\frac{\sqrt{n_3^2 - n_5^2}}{\sqrt{n_1^2 - n_3^2}}\right) \quad \text{(S1)}$$

$$j < \frac{2b}{\lambda}\sqrt{n_1^2 - n_2^2} + 1 - \frac{1}{\pi}\arctan\left(\frac{\sqrt{n_2^2 - n_4^2}}{\sqrt{n_1^2 - n_2^2}}\right) \quad \text{(S2)}$$

where $a(b)$ is the width(thickness) of the waveguide core and i, j are the orders of TE mode (≥ 1). When substituting $n_3 = n_5, n_4 = 1, n_2 = 1.4, n_1 = 3.42$, and $i = j = 1$ (fundamental TE mode) into Equation S1, the inequality is always valid regardless of a value. For Equation S2, with wavelength set as 7.1 μm, we have $b > 110\,nm$. This is in good agreement with the above simulation results.

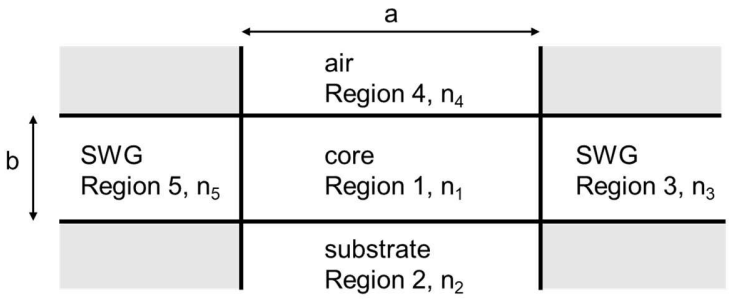

Figure S10. Cross-section of the waveguide regions based on Marcatili's method.

It is noted that the weaker optical mode confinement in a thinner waveguide simultaneously leads to higher scattering loss, which could not be taken into account in the simulation. Thus, the trade-off between absorption and scattering loss practically sets an optimized waveguide thickness for a minimum propagation loss, whose value could be only confirmed by experiment. Meanwhile, a thinner Si device layer weakens the mechanical robustness of the membrane, reducing the size of the membrane that can be transfer-printed and thus the length of the waveguide that can be fabricated. Therefore, the trade-off between waveguide thickness and length also needs to be considered. Nonetheless, the above simulation and calculation results suggest that a small Si waveguide thickness down to a few hundred nanometers could be employed for operating at 6.3-7.1 μm using our SOCF platform. The larger freedom on waveguide thickness makes our SOCF platform more promising for integrated sensing systems compared with those platforms suffering from substrate leakage.

Note S10: Electric field distributions at different wavelengths

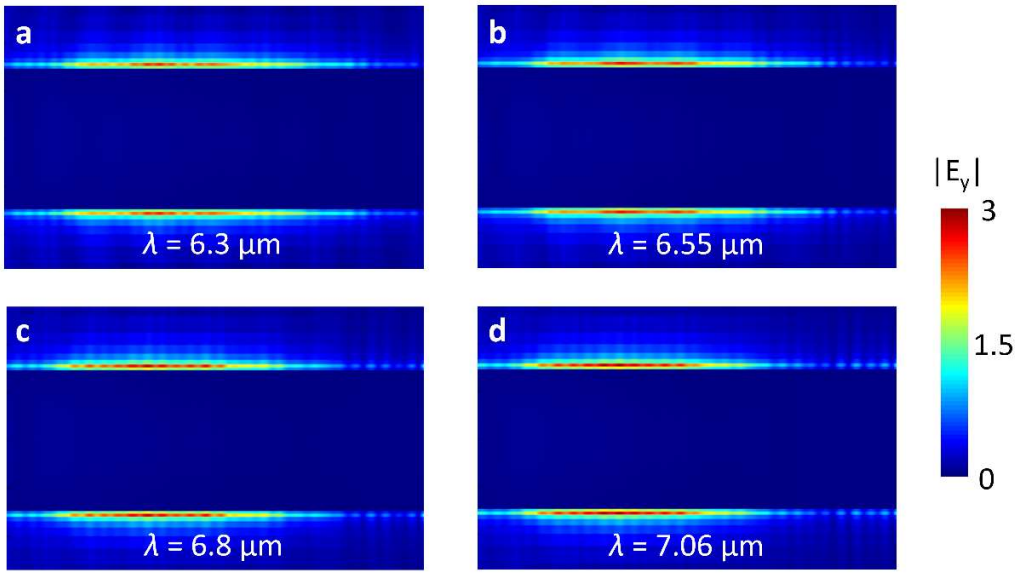

Figure S11. Simulated electric field $|E_y|$ distributions with 1.5 µm wide signal electrode at *xy* plane and at different wavelengths.

Note S11: Graphene photodetector *I-V* curve

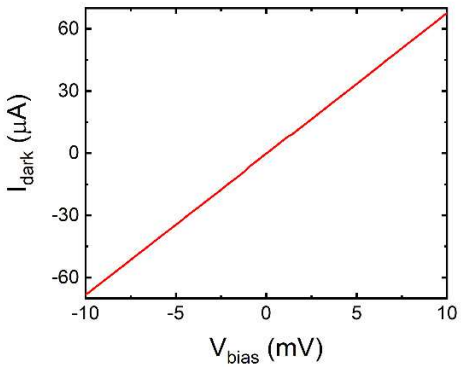

Figure S12. *I-V* curve measured in the former waveguide-integrated graphene photodetector. The linear *I-V* curve confirms good ohmic contact between graphene and metal electrodes and indicates a device resistance of about 150 Ω.

Note S12: Plasmonic hot spots at different wavelengths

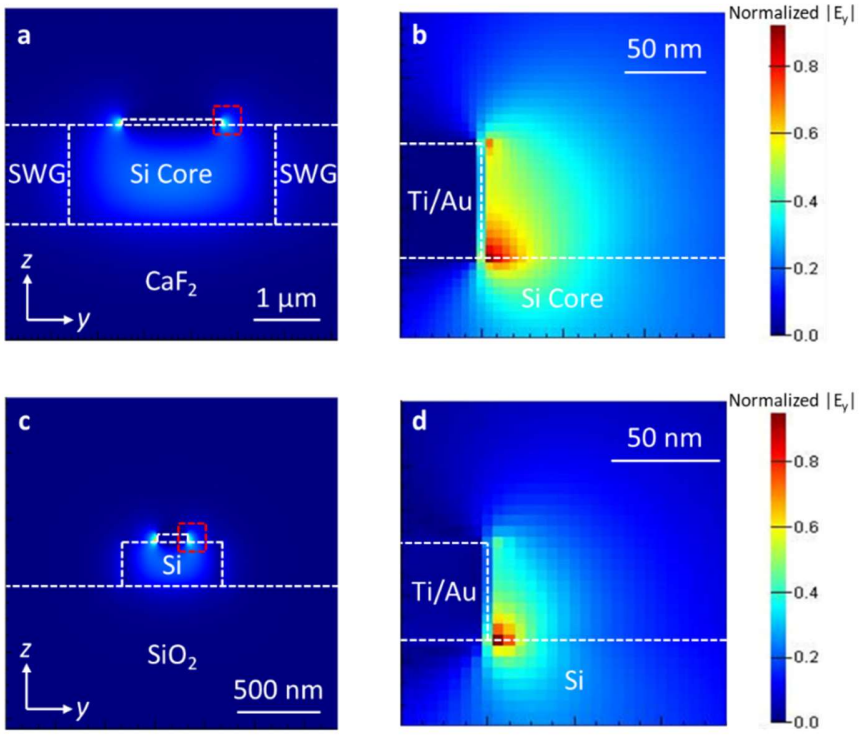

Figure S13. (a) Electric field $|E_y|$ distribution in our device. (b) Zoom-in view of the red dashed box in (a). (c) Electric field $|E_y|$ distribution in the previous work.[3] (d) Zoom-in view of the red dashed box in (c).

Both the electric field intensity in the plasmonic hot spot and the electrostatic potential in the metal-doped graphene junction semi-exponentially decay with the distance from the metal contact edge. The length of the metal-doped graphene junction keeps tens of nanometers,[4,5] while that of the plasmonic hot spot scales with wavelength. As illustrated in Figure R7, the length of the hot spot at the graphene layer is ~70 nm in our device at 6.51 μm and ~30 nm in the previous work employing a similar plasmonic enhancement strategy at 1.55 μm.[3] As a result, compared with the previous work, in our device a lower ratio of the hot spot electrical field overlaps with the large

potential gradient region of the junction, leading to less efficient photocarrier separation and collection. This potentially explains why our simulated graphene absorptance is comparable while our measured responsivity is lower as compared with the previous work.

Note S13: Graphene photodetector for sensing demonstration

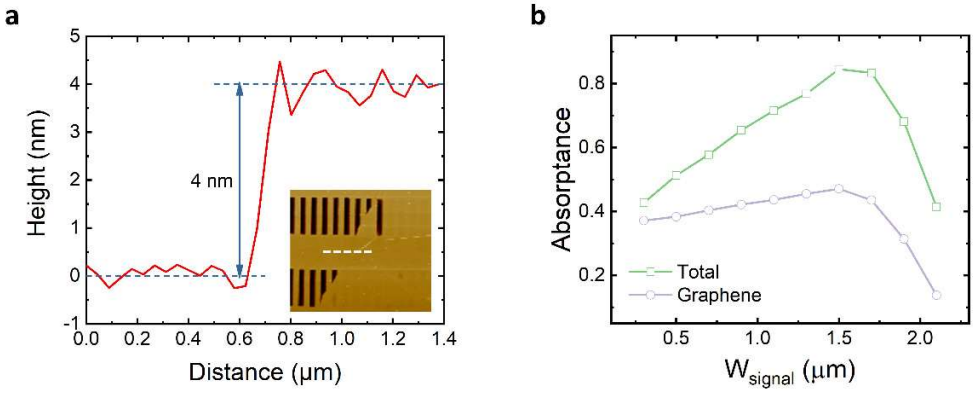

Figure S14. (a) AFM height profile of the graphene flake in the latter waveguide-integrated graphene photodetector for sensing demonstration. Inset shows the AFM image. The white dotted line indicates the cross-section to measure the flake thickness. (b) Simulated graphene and total absorptances at different signal electrode widths and at a signal electrode thickness of 70 nm.

Note S14: Measurement setup

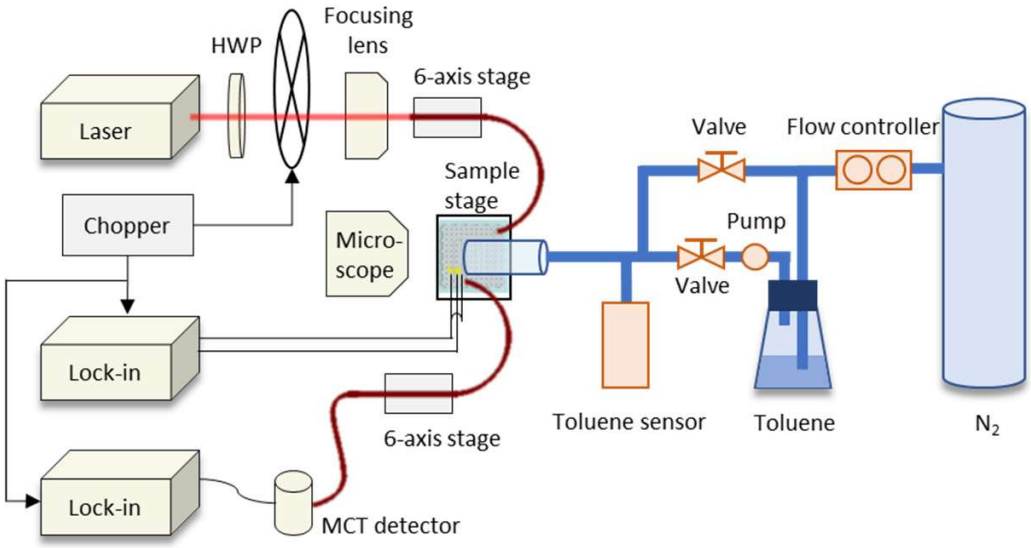

Figure S15. Schematic illustration of the measurement setup.

References:

(1) Penadés, J. S.; Sánchez-Postigo, A.; Nedeljkovic, M.; Ortega-Moñux, A.; Wangüemert-Pérez, J. G.; Xu, Y.; Halir, R.; Qu, Z.; Khokhar, A. Z.; Osman, A.; Cao, W.; Littlejohns, C. G.; Cheben, P.; Molina-Fernández, I.; Mashanovich, G. Z. Suspended Silicon Waveguides for Long-Wave Infrared Wavelengths. *Opt. Lett.* **2018**, *43*, 795–798.

(2) Marcatili, E. A. J. Dielectric Rectangular Waveguide and Directional Coupler for Integrated Optics. *Bell Syst. Tech. J.* **1969**, *48*, 2071–2102.

(3) Pospischil, A.; Humer, M.; Furchi, M. M.; Bachmann, D.; Guider, R.; Fromherz, T.; Mueller, T. CMOS-Compatible Graphene Photodetector Covering All Optical Communication Bands. *Nat. Photonics* **2013**, *7*, 892–896.

(4) Khomyakov, P. A.; Starikov, A. A.; Brocks, G.; Kelly, P. J. Nonlinear Screening of Charges Induced in Graphene by Metal Contacts. *Phys. Rev. B* **2010**, *82*, 115437.

(5) Gabor, N. M.; Song, J. C. W.; Ma, Q.; Nair, N. L.; Taychatanapat, T.; Watanabe, K.; Taniguchi, T.; Levitov, L. S.; Jarillo-Herrero, P. Hot Carrier-Assisted Intrinsic Photoresponse in Graphene. *Science* **2011**, *334*, 648–652.